Atomic scale simulations of battery materials

Don Siegel

Mechanical Engineering Dept., Materials Science & Engineering, Applied Physics Program, Michigan Energy Institute, and Joint Center for Energy Storage Research

University of Michigan

UNIVERSITY OF MICHIGAN

4th Skoltech School for Young Scientists
September 15th, 2019
Moscow

Acknowledgements:
S. Yu, J. Sakamoto, N. Dasgupta (UM)
E. Herbert (Mich. Tech.)
J. Wolfenstine, J. Allen (ARL)
J. Nanda, M. Chi, N. Dudney (ORNL)

1

1

Ann Arbor, Michigan, USA

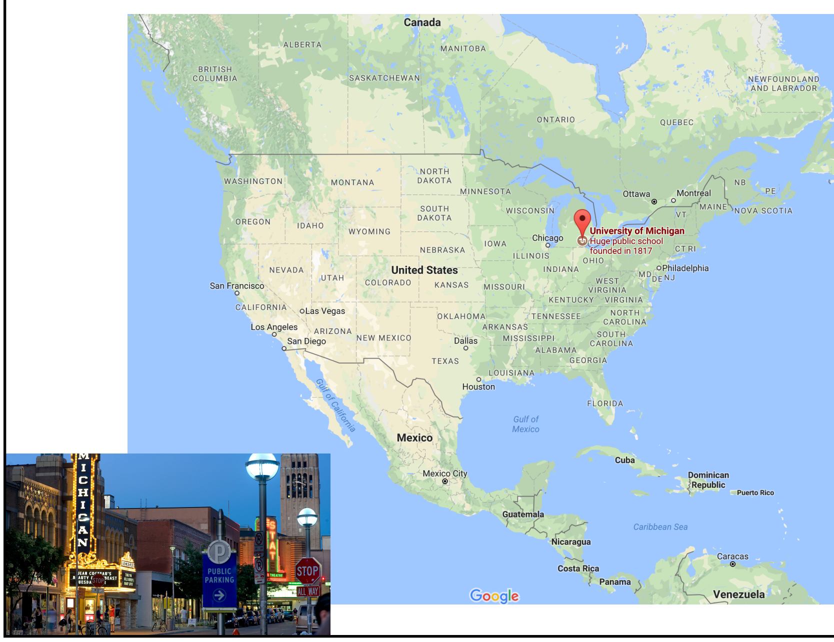

2

2

University of Michigan

3

3

How can computation help?

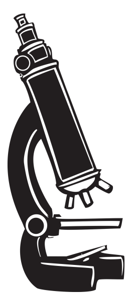

Characterize
Understand

Discover
Predict

4

4

Computational Methods: QM

- **Atomistic computer simulations based on quantum mechanics** (Density Functional Theory)

$$E[n(\mathbf{r})] = T_0[n(\mathbf{r})] + \int V_{\text{ion}}(\mathbf{r})\, n(\mathbf{r})\, d\mathbf{r} + E_{\text{h}}[n(\mathbf{r})] + E_{\text{xc}}[n(\mathbf{r})]$$

- **First-principles approach**:
  - Only empirical input are crystal structure and fundamental physical constants
  - Expensive: requires parallel computation; system sizes generally less than 1,000 atoms
  - Temperature-dependent thermodynamic contributions evaluated within harmonic approximation
    - "Direct method" for construction of dynamical matrix

$$G(T)_{\text{solid}} = H - TS = E_0 + H_{\text{vib}}(T) - S_{\text{vib}}(T)T$$

$$G(T)_{\text{gas}} = H - TS = E_0 + H_{\text{vib}}(T) + \frac{5 + N_{\text{rot}}}{2} k_B T - S_{\exp}(T)T$$

$$H_{\text{vib}}(T) = \sum_i \frac{1}{2}\hbar\omega_i + \hbar\omega_i \left[\exp\left(\frac{\hbar\omega_i}{k_B T}\right) - 1\right]^{-1} \qquad S_{\text{vib}}(T) = k_B \sum_i \frac{\hbar\omega_i / k_B T}{\exp(\hbar\omega_i / k_B T)} - \ln\left[1 - \exp\left(\frac{-\hbar\omega_i}{k_B T}\right)\right]$$

5

5

Computational Methods: Classical

Molecular dynamics allows us to simulate the time-evolution of an atomic system

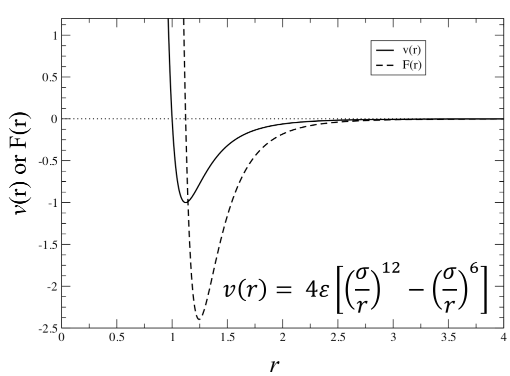

Interactions between atoms are prescribed by an interatomic potential

Time evolution of the system:

$$x(t+\Delta t) = x(t) + v_x(t)\Delta t + \frac{1}{2} a_x(t)\Delta t^2$$

$$v_x(t+\Delta t) = v_x(t) + \frac{1}{2}\left[a_x(t+\Delta t) + a_x(t)\right]\Delta t$$

6

6

Example Calculations

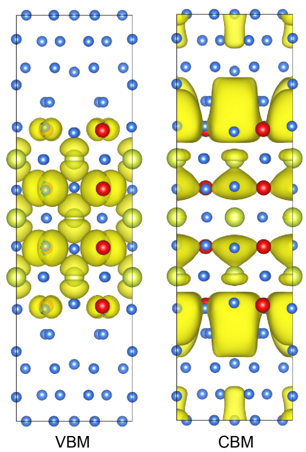

Partial charge density of the VBM and CBM of a Li_3OCl solid electrolyte when in contact with a Li negative electrode

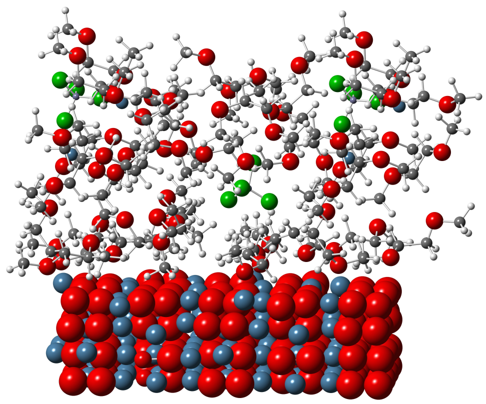

Electrolyte decomposition on Li-air battery cathode

7

7

High-Throughput Screening

~100,000 MOFs computationally evaluated for their hydrogen storage capacity

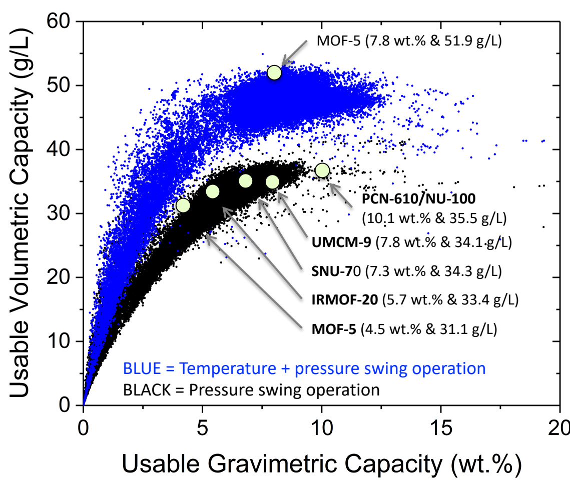

High-throughput Grand Canonical Monte Carlo calculations

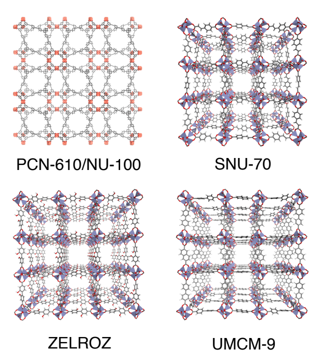

Ahmed et al., *Balancing Gravimetric and Volumetric Hydrogen Density in MOFs,* Energy & Environmental Science, **10**, 2459 (2017) DOI: 10.1039/C7EE02477K
Ahmed et al., *Exceptional Hydrogen Storage Achieved by Screening Nearly Half a Million Metal-Organic Frameworks,* Nature Communications, (2019) DOI: 10.1038/s41467-019-09365-w

8

Introduction: Li-ion Batteries

The Good: High capacity, voltage, specific energy[1]

The Bad: Safety issues resulting from use of liquid electrolytes

- Liquid electrolytes are volatile, flammable, and prone to dendrite formation[2,3]

Swollen battery[4]

Tesla model S fire (2013)[6]

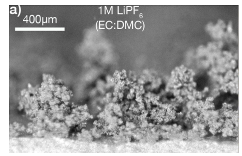

Dendrite observation[8]

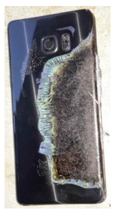

Samsung galaxy note 7 recall (2016)[5]

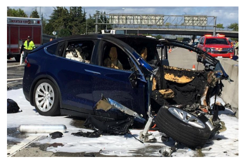

Tesla model X fire (2018)[7]

[1] M. Dimitrijevic, *Lithium Ion Battery Assembly Challenges.* ECN (**2011**). (http://www.ecnmag.com/articles/2011/01/lithium-ion-battery-assembly-challenges)
[2] Roth, E. P.; Orendorff, C. J. How Electrolytes Influence Battery Safety. *Electrochem. Soc. Interface* **2012**, *21* (2), 45–49.
[3] Goodenough, J. B.; Singh, P. Review—Solid Electrolytes in Rechargeable Electrochemical Cells. *J. Electrochem. Soc.* **2015**, *162* (14), A2387–A2392.
[4] P. Lee, *Dealing with swollen batteries* (**2016**). (http://www.computerhowtoguide.com/2016/05/dealing-swollen-batteries.html)
[5] B. Petrovan, *Galaxy Note 7 recall*, Android Authority (**2016**). (http://www.androidauthority.com/samsung-galaxy-note-7-recall-714419/)
[6] W. Oremus, *Tesla Catches Fire, Feds Can't Investigate Due to Shutdown* (**2013**). (http://www.slate.com/blogs/future_tense/2013/10/03/tesla_fire_video_nhtsa_can_t_investigate_model_s_battery_fire_due_to_shutdown.html)
[7] D. Shepardson, *U.S. opens prove into fatal Tesla crash, fire in California* (**2018**). (https://www.reuters.com/article/us-tesla-crash-ntsb/u-s-opens-probe-into-fatal-tesla-crash-fire-in-california-idUSKBN1H32O1)
[8] Wood, K. N.; Kazyak, E.; Chadwick, A. F.; Chen, K-H.; Zhang, J-G.; Thornton, K.; Dasgupta, N. P. Dendrites and Pits: Untangling the Complex Behavior of Lithium Metal Anodes through Operando Video Microscopy. ACS Cent. Sci. **2016**, *2* (11), 790–801.

9

Why Li-metal Anodes Aren't Used Today

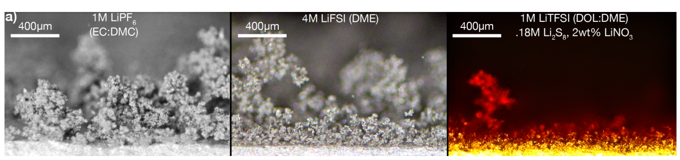

Comparison of three very different electrolyte systems ($LiPF_6$, LiFSI, and LiTFSI). (a) Visualization cell images after 900 s of deposition at 5 mA cm^{-2}. A clear difference in dendrite size, nucleation density, and surface coverage is observed.

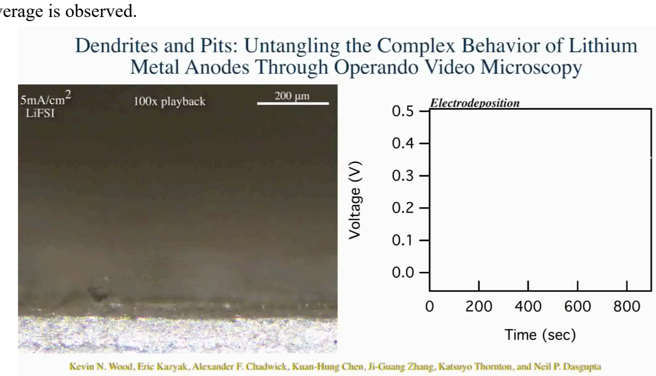

Wood et al., *ACS Cent. Sci.*, **2016**, *2*, 790–801

10

10

Solid electrolytes

- **Advantages of solid electrolytes:**
  - Less flammable and non-volatile[1]
  - High stiffness: Suppression of dendrites[2]
    ➔ Metallic Li anode (high capacity)
  - Resistance to changes in temperature
- **Requirements:**
  - $\sigma_{Li} > 10^{-4}$ S/cm [4]
    : $Li_7La_3Zr_2O_{12}$,[5] $Li_{10}GeP_2S_{12}$,[6] etc.
  - Interfacial stability
  - Resistance to dendrite penetration

Comparison of Li-ion and lithium metal cells[3]

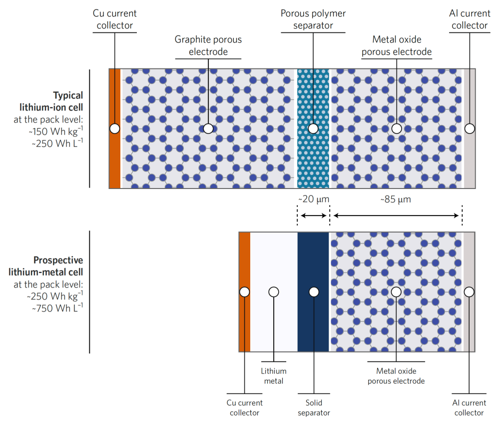

Although a growing number of ionically-conducting solids are known, essentially all exhibit shortcomings such as limited interfacial stability and susceptibility to dendrite penetration.

[1] Hu, Y.-S., *Nat. Energy* **2016**, *1* (4), 16042.
[2] Monroe C.; Newman, J. J., Electrochem. Soc. **2005**, *152* (2), A396–A404.
[3] Albertus, P.; Babinec, S.; Litzelman, S.; Newman, A., *Nat. Energy* **2018**, *3* (1), 16–21.
[4] Goodenough, J. B.; Kim, Y., *Chem. Mater.* **2010**, *22* (3), 587–603.
[5] Murugan, R. et al., *Angew. Chemie - Int. Ed.* **2007**, *46* (41), 7778–7781.
[6] Kamaya, N. et al., *Nat. Mater.* **2011**, *10* (9), 682–686.

11

Useful for Many Types of Batteries

Solid electrolytes: a unifying technology for *Beyond Li-ion* Batteries

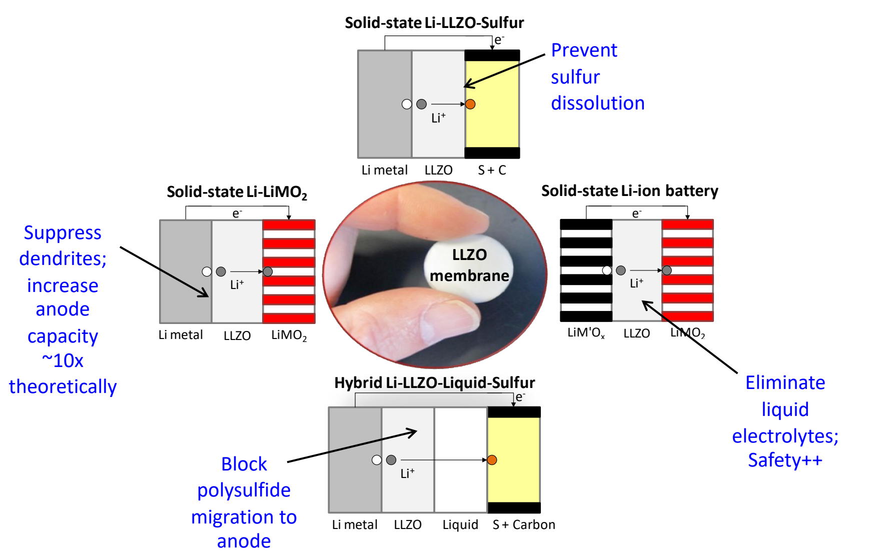

12

12

LLZO: A Promising Solid Electrolyte

Nominal composition: $Li_7La_3Zr_2O_{12}$
Li-ion conductivity: ~5×10^{-4} S/cm

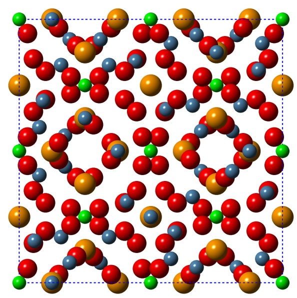

Cubic unit cell
192 atoms ☹

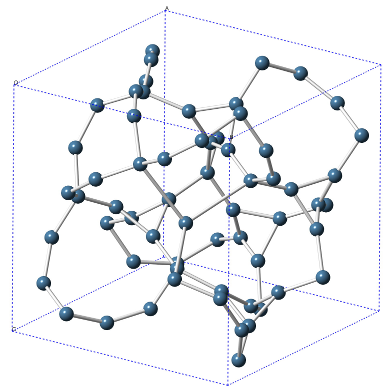

Partially-occupied lithium sub-lattice
3D, percolating

13

13

Electrochemical Window

Electrolyte stability is determined by the position of the electrolyte's energy levels with respect to the redox levels of the electrodes (μ_A & μ_C)

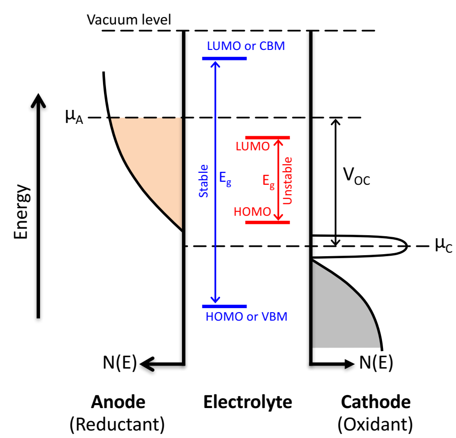

For stability, we desire:
μ_A < CBM
μ_C > VBM

HOMO = Highest Occupied Molecular Orbital
LUMO = Lowest Unoccupied Molecular Orbital
CBM = Conduction Band Minimum
VBM = Valence Band Maximum

14

14

LLZO: Stable Against Li Metal

LLZO has a large band gap, 6.4 eV, (GW method) but its effective electrochemical window is approximately 4 V

Equilibrium with Anode | **Equilibrium with Cathode**

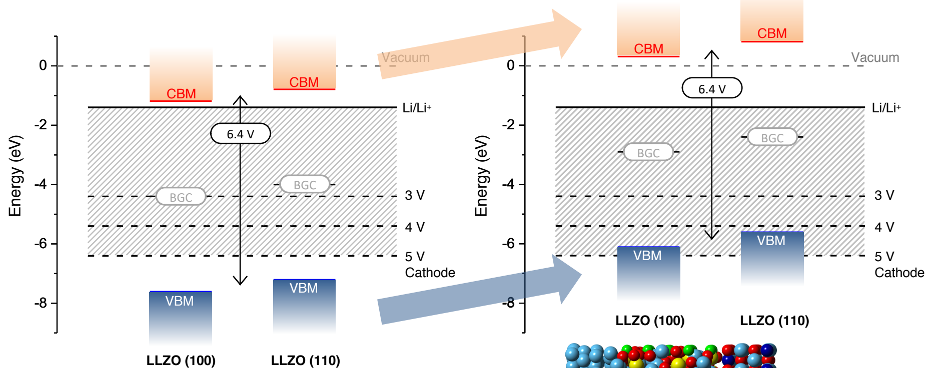

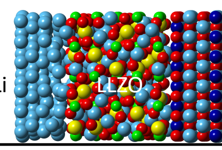

T. Thompson et al., *Electrochemical Window of the Li-Ion Solid Electrolyte $Li_7La_3Zr_2O_{12}$*
ACS Energy Lett. 2017, 2, 462−468

15

15

Topics

Goal: Understand phenomena that limit the performance of LLZO-based batteries.

This knowledge can be used to design viable solid electrolytes.

Elastic Properties

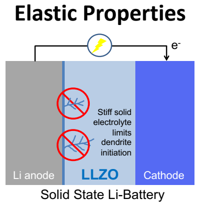

Grain Boundary Transport

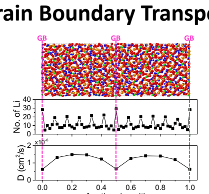

Low-Resistance Interfaces

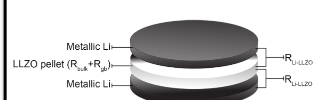

10.1021/acs.chemmater.5b03854
10.1021/acsami.8b17223

10.1021/acs.chemmater.7b02805

10.1021/acs.chemmater.7b03002
10.1039/c7ta03162a

16

16

Elastic Properties of LLZO

- Monroe and Newman[1] proposed a finite element model for dendrite initiation at the interface between a negative electrode and a solid electrolyte (SE)
  - Dendrite suppression depends on the elastic properties of the SE
  - **SE having a shear modulus (G) twice that of Li should suppress dendrites**

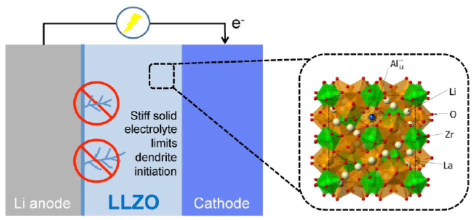

Solid State Li-Battery

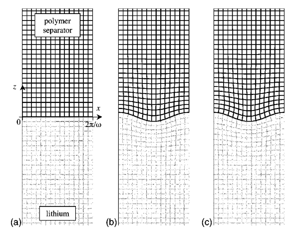

The Impact of Elastic Deformation on Deposition Kinetics at Lithium/Polymer Interfaces

Charles Monroe**,z and John Newman**

- Few studies of the mechanical properties of LLZO have been reported
  - We determine the elastic constants and moduli (Young's modulus, shear modulus, and bulk modulus) for Al- and Ta-doped LLZO

[1] C. Monroe & J. Newman. The Impact of Elastic Deformation on Deposition Kinetics at Lithium/Polymer Interfaces. *J. Electrochem. Soc.* 2005, *152*, A396-A404.

17

17

Approach & Goals

- **Goal:** Determine if LLZO has sufficient stiffness to suppress dendrite initiation
- **Approach:** Evaluate elastic properties and compare with Monroe/Newman model predictions
- **Methods:** Elastic constants and moduli of LLZO were evaluated using 3 techniques:
  - First-principles calculations
  - Acoustic impulse excitation measurements
  - Nanoindentation experiments

18

18

Calculation Method

- Calculations were performed using Density Functional Theory with a plane wave basis and the projector augmented wave method (VASP code)
- The PBE generalized gradient approximation was used for the exchange correlation energy

Strain tensor

$$\varepsilon = \begin{bmatrix} \delta & 0 & 0 \\ 0 & -\delta & 0 \\ 0 & 0 & \delta^2/(1-\delta^2) \end{bmatrix}$$

Undistorted supercell

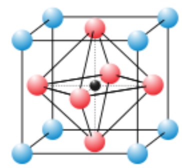

Distorted supercell

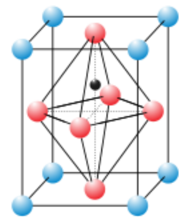

Resolved shear modulus

$$G_{[100]} = C_{44},$$
$$G_{[110]} = \frac{2(C_{11}-C_{12})C_{44}}{C_{11}-C_{12}+2C_{44}},$$
$$G_{[111]} = \frac{3(C_{11}-C_{12})C_{44}}{C_{11}-C_{12}+4C_{44}}$$

Polycrystalline, isotropic moduli (Voigt–Reuss–Hill averaging scheme):[1,2]

$$G = \frac{1}{2}\left[\frac{C_{11}-C_{12}+3C_{44}}{5} + \frac{5C_{44}(C_{11}-C_{12})}{4C_{44}+3(C_{11}-C_{12})}\right]$$

$$E = \frac{9GB}{3B+G}, \quad \nu = \frac{3B-2G}{2(3B+G)}$$

(1) Chung, et al., J. Am. Ceram. Soc. 1963, 46, 452. (2) Uesugi, et al., Mater. Trans. 2005, 46, 1117

19

19

Calculated Energy vs. Distortion

Elastic constants are determined by fitting a polynomial to energy vs. strain data

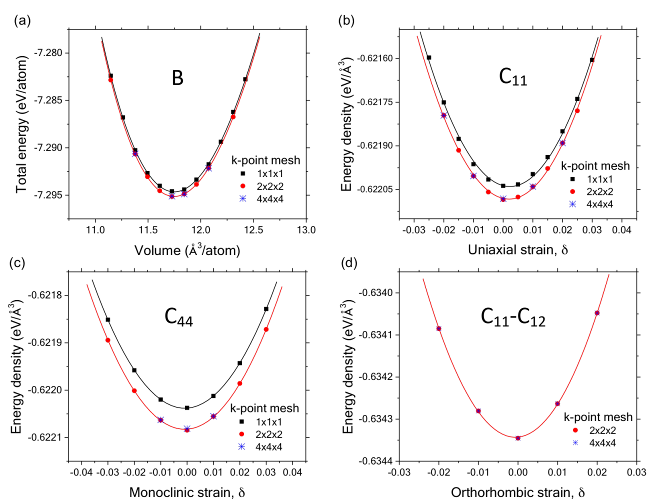

Figure 2. Calculated total energy (or energy density) of Al-doped LLZO as a function of the (a) cell volume, (b) uniaxial strain, (c) monoclinic strain, and (d) orthorhombic strain.

20

20

Materials Characterization

LLZO samples examined have low porosity and contain few 2nd phase impurities

XRD patterns are consistent with a pure cubic structure with no second phases

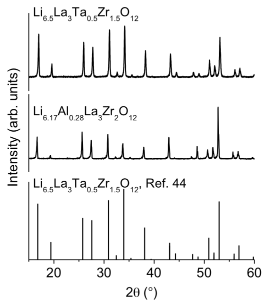

Figure 3. X-ray diffraction patterns of Al-doped and Ta-doped LLZO.

SEM fractography was used to evaluate the amount and distribution of porosity. The relative density for both compositions approaches the theoretical density, 98.9%.

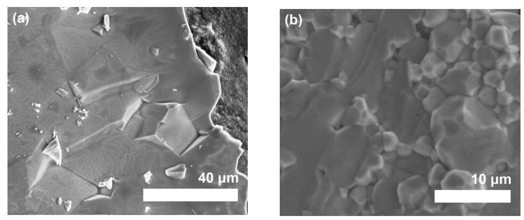

Figure 4. Fracture surfaces of: (a) Al-doped and (b) Ta-doped LLZO.

21

21

Measured Young's Modulus

Young's modulus, measured by nano-indentation, is insensitive to dopant composition

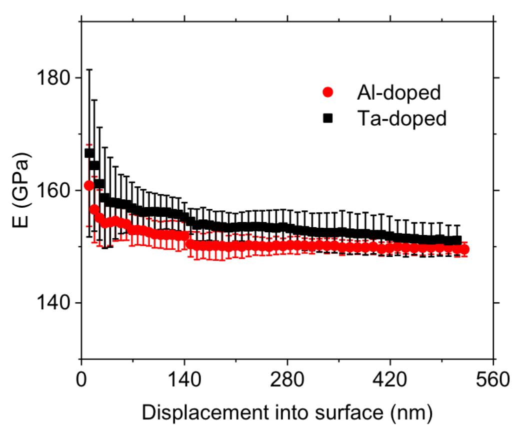

Figure 5. Young's modulus, *E*, of Al-doped and Ta-doped LLZO specimens as a function of nanoindentation displacement.

Erik Herbert, Michigan Tech.

22

22

LLZO Elastic Properties

The calculated and measured isotropic shear modulus are in good agreement, and fall within the range of 56 to 61 GPa.

Table 1. Elastic properties of Al-doped and Ta-doped LLZO. The elastic constants and moduli are expressed in GPa.

	C_{11}	C_{12}	C_{44}	B	E	G	ν
Al-doped LLZO							
DFT (0 K)	187.0	75.1	71.0	112.4	162.6	64.6	0.26
DFT extrapolated (298 K)					154.5	61.4	
Impulse excitation (298 K)				100.2 ± 0.6	146.1 ± 0.8	58.1 ± 0.3	
Dynamic nanoindentation (298 K)					150.3 ± 2.2	59.8 ± 0.9	
RUS (298 K) Ref. 21				102.8 ± 0.3	149.8 ± 0.4	59.6 ± 0.1	0.257±0.002
Ta-doped LLZO							
DFT (0 K)	169.8	63.9	69.8	99.2	154.9	62.5	0.24
DFT extrapolated (298 K)					147.2	59.4	
Impulse excitation (298 K)				96.0 ± 1.4	139.9 ± 2.1	55.7 ± 0.8	
Dynamic nanoindentation (298 K)					153.8 ± 2.7	61.2 ± 1.1	

Li Elastic Properties

Also re-evaluated the properties of BCC lithium.
(Useful data for macro-scale mechanical models of Li.)

Table 2. Elastic properties of BCC Li. The elastic constants and moduli are expressed in GPa. Values marked with an asterisk are derived using Eq. (6) and (7). DFT values were extrapolated to 298 K by reducing the zero Kelvin values by 15%.

	B	C_{11}	C_{12}	C_{44}	E	G	ν
Zero Kelvin							
DFT (present study)	13.7	15.3	12.8	11.3	13.0	5.0	0.34
Experiment Ref. 50	13.8	15.4	13.0	11.3	12.9*	4.9*	
Experiment Ref. 51	13.2	14.7	12.5	11.3	12.6*	4.8*	
Experiment Ref. 52	13.1	14.6	12.4	11.4	12.6*	4.8*	
298 Kelvin							
DFT (present study)					11.1	4.25	
Experiment Ref. 51	12.0	13.4	11.3	8.9	10.6*	4.0*	
Experiment Ref. 52	11.9	13.3	11.2	8.8	10.5*	4.0*	
Experiment Ref. 53	12.0	13.4	11.3	8.8	10.5*	4.0*	
Experiment Ref. 54					8.0		
Experiment Ref. 55					4.9		

Li has anisotropic elastic properties

$E_{[100]}$	$E_{[110]}$	$E_{[111]}$	$G_{[100]}$	$G_{[110]}$	$G_{[111]}$
Zero Kelvin					
3.6	10.3	26.6	11.3	2.2	1.8
298 Kelvin					
3.1	8.8	22.6	9.6	1.9	1.5

S. Yu et al., Elastic Properties of the Solid Electrolyte $Li_7La_3Zr_2O_{12}$ (LLZO)
Chemistry of Materials. 2016, 28, 197–206

Summary: Elastic Properties

- Monroe/Newman: SE with shear modulus (G) twice that of Li should suppress dendrites
  - G for Li: 4.25 GPa
  - SE having G of ~8.5 GPa is required to suppress dendrites
  - G for LLZO: 58-60 GPa (10x the shear modulus of Li)
- LLZO is expected to suppress dendrite formation
- Nevertheless, dendrites could still form even with an SE that satisfies Monroe's criterion
  - Monroe/Newman neglects microstructural effects: Eg., porosity at the electrolyte/anode interface could be problematic
  - High stiffness should be viewed as a *necessary, but not sufficient condition for a viable solid electrolyte*

S. Yu et al., Elastic Properties of the Solid Electrolyte $Li_7La_3Zr_2O_{12}$ (LLZO)
Chemistry of Materials. 2016, 28, 197–206

25

25

Dendrites?!

Microstructural features, and not elastic properties alone, are important in the design of solid electrolytes

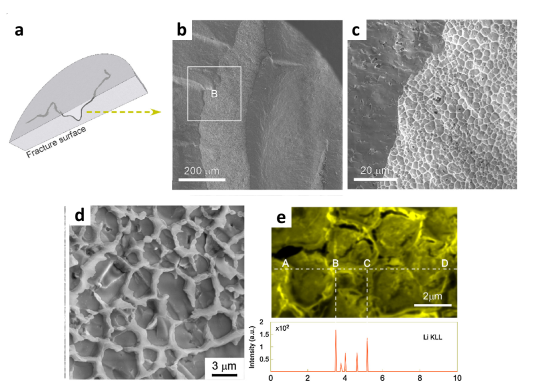

Figure. SEM and Auger analysis of the Li "web structure" within a cycled, short-circuited LLZO pellet. (a) Cartoon of a fracture surface that intersects one of the black linear features; (b) SEM image of the fracture surface; (c) magnification of the boxed area "B" in (b), with the right portion of the image intersecting the black linear feature; (c-d) higher magnification of the black feature, showing its web-like structure; (e) Auger line scan for Li across the web-like structure, revealing it to be metallic lithium.

- Short circuiting observed in Li-LLZO-Li symmetric cells at room temperature for current densities > 0.05 mA/cm^2
- LLZO membranes develop black, linear features that propagate across entire membrane
- These features are metallic Li, and coincide with the location of grain boundaries

Sakamoto group:
10.1016/j.electacta.2016.12.018

26

26

Inhomogeneities

While the model of Monroe and Newman is a helpful starting point, it assumes that the solid electrolyte (SE) is ***homogeneous.***

→ However, a practical SE will not be homogeneous: inhomogeneities are introduced by microstructural features such as grain boundaries, surface phases, pores, cracks, etc.

How can inhomogeneities in a SE impact dendrite formation?

27

27

Mechanisms of Inhomogeneous Plating

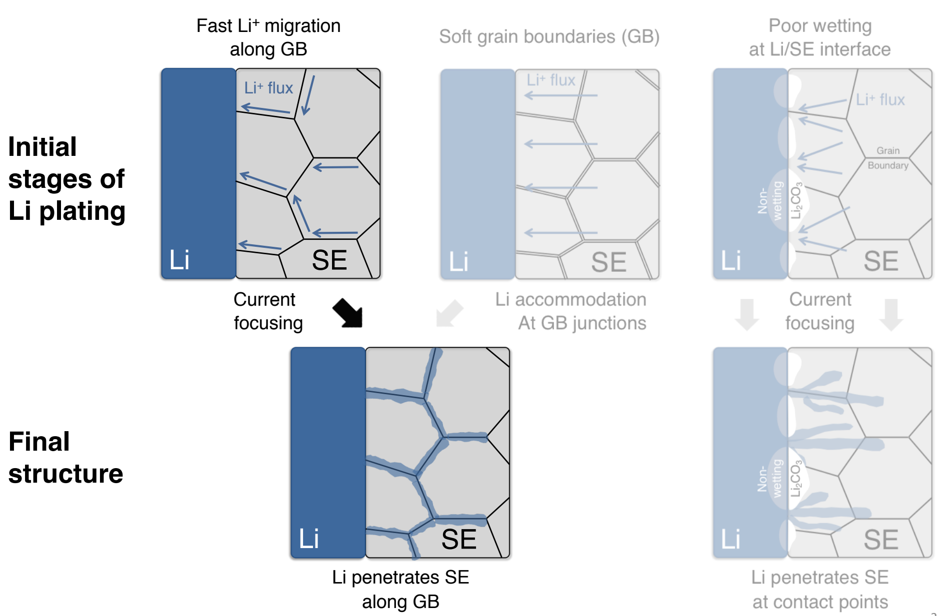

28

28

Overview: Grain Boundaries

Can fast GB transport create 'hot spots' (i.e., nucleate dendrites) during plating?

- GB transport in polycrystalline oxides can be fast or slow:
  - In Al_2O_3[1], HfO_2,[2] and UO_2[3] ionic diffusion is **enhanced** at GBs
  - In $SrTiO_3$[4], YSZ,[5] and doped CeO_2[6] GBs **hinder** ion transport
- In LLZO, GB resistance can decrease Li^+ conductivity.[7-12]
  - GB contribution comprises 26% of the total resistance for LLZO samples hot pressed at 1000°C.[11]
  - GB impact can be minimized by altering synthesis conditions: increasing density, increasing grain size, and/or improving contact at GBs.[11-12]
- Despite the importance of GBs, the atomic-scale processes occurring at GB in LLZO remain poorly understood
- We combine Monte Carlo (MC) and molecular dynamics (MD) simulations to predict the energetics, composition, and transport properties in three model, low-energy symmetric tilt GBs in LLZO

(1) T. Nakagawa et al., J. Ceram. Soc. Jpn.; 2006.
(2) McKenna et al., Appl. Phys. Lett. 2009, 95, 222111.
(3) Williams et al., J. Nucl. Mater. 2015, 458, 45-55.
(4) Metlenko et al., Nanoscale 2014, 6, 12864-12876.
(5) De Souza et al., Phys. Chem. Chem. Phys. 2008, 10, 2067-2072.
(6) Sun et al., Nat. Commun. 2015, 6, 6294.
(7) Ohta et al, *J. Power Sources* **2014,** *265*, 40-44.
(8) Li et al., *J. Power Sources* **2014,** *248*, 642-646.
(9) El Shinawi et al., *J. Power Sources* **2013,** *225*, 13-19.
(10) Tenhaeff et al., *ChemElectroChem* **2014,** *1*, 375-378.
(11) David et al., *J. Am. Ceram. Soc.* **2015,** *98*, 1209-1214.
(12) Thompson et al., *Adv. Energy Mater.* **2015,** *5*, 1500096.

29

29

Grain Boundary Models

We examined Li^+ transport along three low-energy GBs

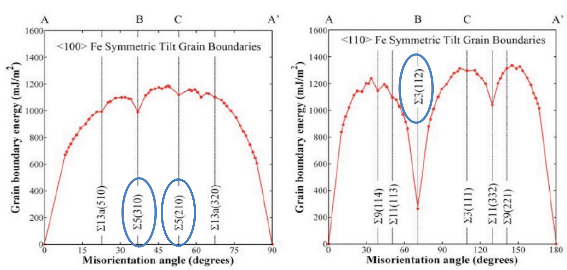

Phys. Rev. B **85**, 064108 (2012)

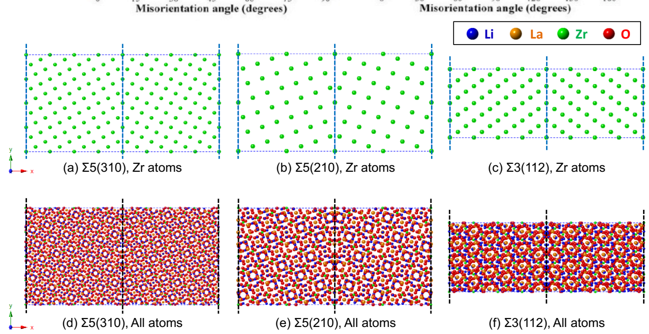

(a) Σ5(310), Zr atoms (b) Σ5(210), Zr atoms (c) Σ3(112), Zr atoms

(d) Σ5(310), All atoms (e) Σ5(210), All atoms (f) Σ3(112), All atoms

30

30

Methodology

Geometry optimization
↓
MD heating to target temperature (800 to1100 K)
↓
MD equilibration at target temperature
↓
Monte Carlo equilibration at target temperature
↓
Calculate mean squared displacement (MSD) with MD at target temperature

- Molecular dynamics and Monte Carlo simulations were conducted using LAMMPS[1]
  - Simulation cells: ~2000 to ~15,000 atoms
- All calculations performed using a Morse-type force-field derived from *softBV* bond valence parameters[2-3]
  - Prior calculations with this force field yielded good agreement with measured static and dynamic properties of LLZO[3-4]

Diffusion coefficient:

$$D = \frac{1}{2dt}\langle[\boldsymbol{r}(t+t_0) - \boldsymbol{r}(t_0)]^2\rangle$$

1. Plimpton, S. J. Comput. Phys 1995, 117, 1-19
2. Adams, S.; Rao, R. P. *Phys. Status Solidi A* **2011,** *208*, 1746-1753.
3. Adams, S.; Rao, R. P. *J. Mater. Chem.* **2012,** *22*, 1426-1434.
4. Yow, Z. et al., *Solid State Ionics* **2016,** *292*, 122-129.

31

31

GB Composition

GBs are predicted to be enriched with lithium, and to a smaller extent with oxygen

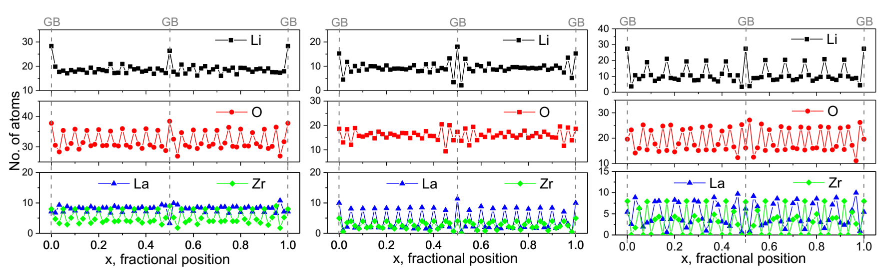

(a) Σ5(310) (b) Σ5(210) (c) Σ3(112)

Figure. Calculated average composition of Li (black), O (red), La (blue), and Zr (green) as a function of position normal to the GB plane (x axis) at 1000 K for supercells containing (a) Σ5(310), (b) Σ5(210), and (c) Σ3(112) GBs. Vertical dashed lines indicate the positions of the GB planes (at x = 0 or 1 and 0.5).

32

32

Li-ion Trajectories

Li-ion diffusion is slowed near GBs

Full cell

GB region

Bulk region

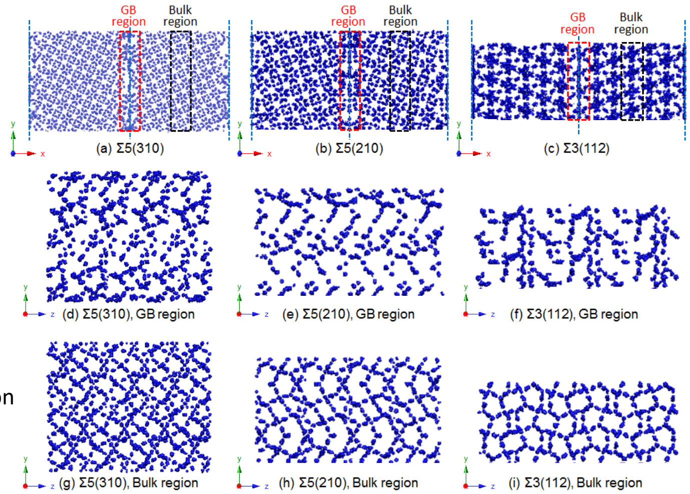

Fragmented

Continuous

Figure. Li-ion trajectories for the GB simulation cells plotted over a 5 ns MD window at 700 K: (a-c) view along the GB tilt axis (z direction); (d-f) view normal to the GB plane (x direction) for a region centered on the GB (0.45<x<0.55) corresponding to the red dashed boxes in (a-c); (g-i) view normal to GB plane for a bulk region (0.7<x<0.8) corresponding to the black dashed boxes in (a-c).

33

33

Diffusivity

Diffusion at GBs is generally slower than in bulk LLZO

Total diffusivity

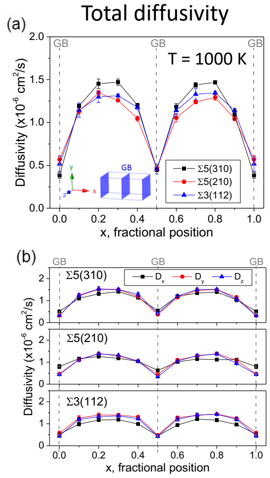

Little GB diffusion anisotropy at 1000 K

Li ion diffusivity as a function of position: (a) total diffusivity (b) diffusivity projected along x, y, z

Calculated diffusivities and activation energies

System	1000 K (10^{-7} cm²/s)		300 K (extrapolated) (10^{-13} cm²/s)			
	D	E_a (eV)	D	D_x	D_y	D_z
Bulk	13.5	0.52	9.16			
Σ5(310)	4.30	0.64	0.15	0.11	0.10	0.28
Σ5(210)	5.50	0.71	0.03	0.05	0.02	0.02
Σ3(112)	5.10	0.52	4.71	0.04	40.0	8.12

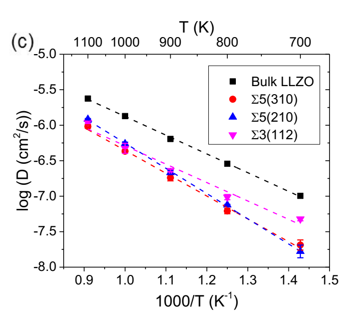

34

34

Summary: GB Transport

No evidence for fast transport in LLZO GBs

- MC and MD simulations were used to predict the energetics, composition, mobility, and transport properties of three model, low-energy GBs in LLZO
- Calculations predict:
  - GB plane is enriched with Li and O
  - GB diffusion depends on GB structure (excess volume)
    - Open GB's are slower than bulk
    - Compact boundaries have similar diffusivity to bulk
  - Evidence for anisotropic diffusion at RT in compact boundaries

Current-focusing at GB/electrode junctions (hot spots) is not responsible for Li dendrite initiation

Yu and Siegel, Grain Boundary Contributions to Li-ion Transport in the Solid Electrolyte $Li_7La_3Zr_2O_{12}$ (LLZO)
Chemistry of Materials, **29**, 9636-9647 (2017). DOI: 10.1021/acs.chemmater.7b02805

35

35

Mechanisms of Inhomogeneous Li Deposition

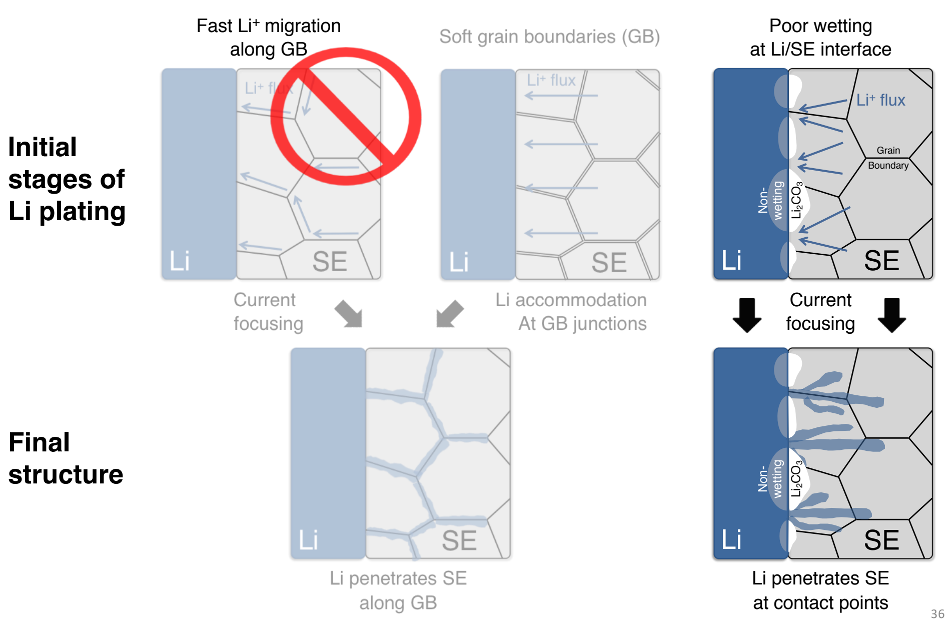

36

36

Surface Contamination & Interfacial Resistance

Cell assembled immediately after cleaning

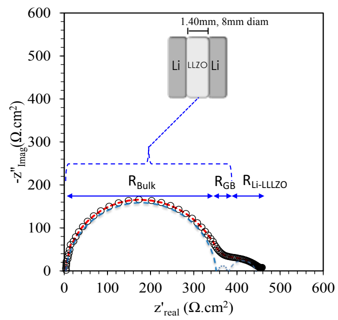

Cell assembled after 10 days air exposure

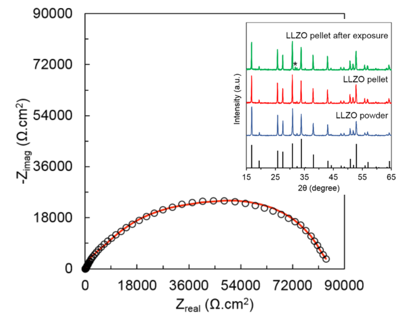

- Significant increase in $R_{Li\text{-}LLZO}$ after air exposure (R_{bulk} & R_{GB} unchanged)
- Surface contaminants form: Li_2CO_3 and LiOH
- Reversible Li+/H+ exchange in humid environments[1]

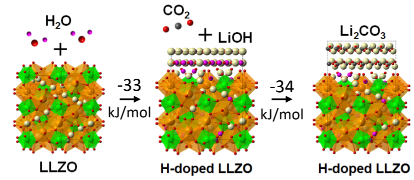

Sharafi *et al.*, *Impact of Air Exposure and Surface Chemistry on Li-Li7La3Zr2O12 Interfacial Resistance*, J. Mater. Chem. A, 5, 13475 (2017).

[1] Ma, C., et al. *Angew. Chem.* (2015) 127, 1, 131-135.

37

37

Interfacial Wetting

Removal of surface Li_2CO_3 (and LiOH) greatly increases the wetting of LLZO by Li

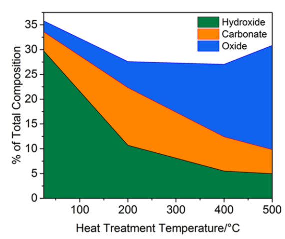

Fig. 1. Percentage of total composition of oxygen-containing species (from XPS) on the LLZO surface vs heat treatment temperature after wet polishing (WP) with a glycol-based diamond paste

$$W_{ad} = \sigma_{Li} (1 + \cos \theta)$$

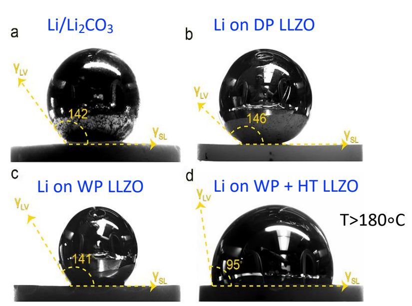

Fig. 2 Contact angle measurements of molten metallic Li on a) Li_2CO_3, b) DP-LLZO, c) WP-LLZO, d) WP-LLZO after heat treatment at 500°C.

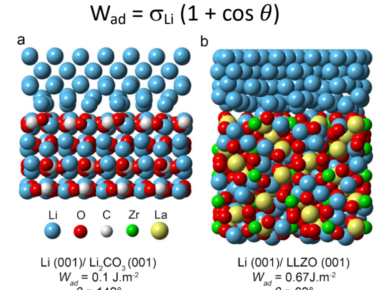

Figure 3. Calculated work of adhesion (W_{ad}), contact angle (θ), and atomic structure for the a) Li-Li_2CO_3 and b) Li-LLZO interfaces.

38

38

Ultra-Low Interface Resistance

Enhanced wetting achieved with WP+HT correlates with very low interfacial resistance and 6x increase in critical current density

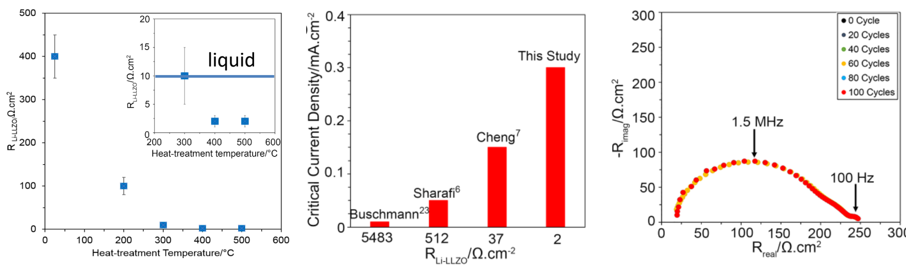

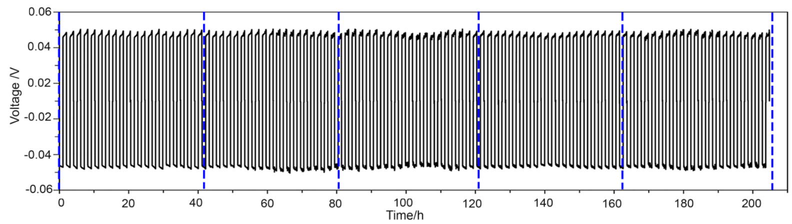

40

40

Conclusion: Low-Resistance Interfaces

- The interfacial resistance of LLZO against Li metal can be reduced to 2 Ω.cm^2 – lower than that of liquid electrolytes – by controlling the surface chemistry of LLZO and *without* interfacial coatings
- This low resistance is rationalized in terms of the interfacial chemistry, which impacts Li wettability and electrochemical performance
  - The presence of surface contaminants, Li_2CO_3 and LiOH, results in poor wettability and high interfacial resistance
- A procedure for removing harmful surface layers is demonstrated
  - Dramatic increase in Li wetting and the elimination of nearly all interfacial resistance
  - Favorable interfacial properties are maintained over one hundred cycles, and suggest a pathway to achieving efficient solid-state batteries

Sharafi *et al., Surface Chemistry Mechanism of Ultra-Low Interfacial Resistance in the Solid-State Electrolyte* $Li_7La_3Zr_2O_{12}$
Chemistry of Materials, 29, 7961-7968 (2017).
DOI: 10.1021/acs.chemmater.7b03002

41

41

Mechanisms of Inhomogeneous Plating

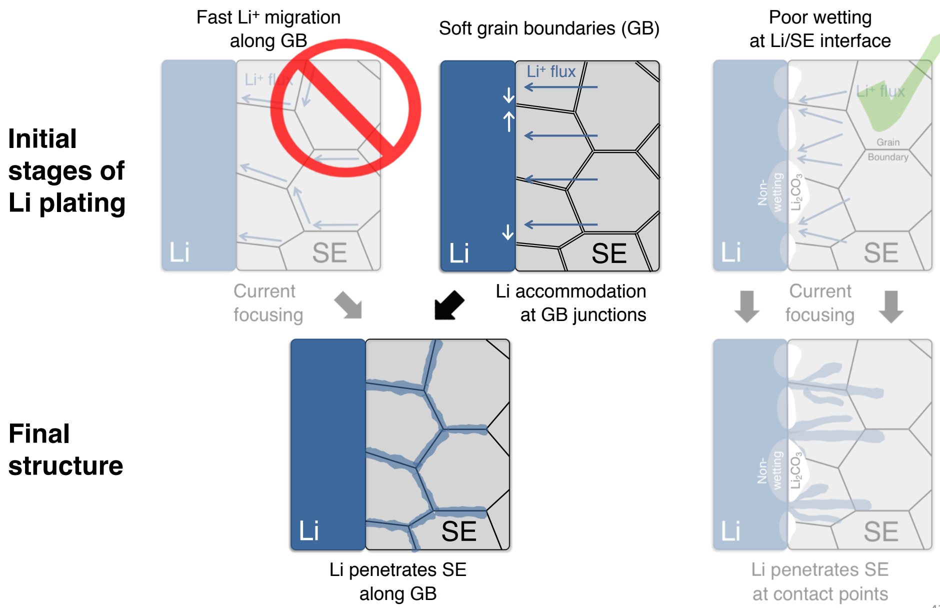

42

42

Subway Analogy

Options presented to a Li-ion as it deposits on the Li electrode surface

Which train do you want to get on?

Stiff, dense interfacial regions

Regions with voids, cracks, soft spots

43

43

GB Softening

Are GBs in LLZO softer than the bulk?

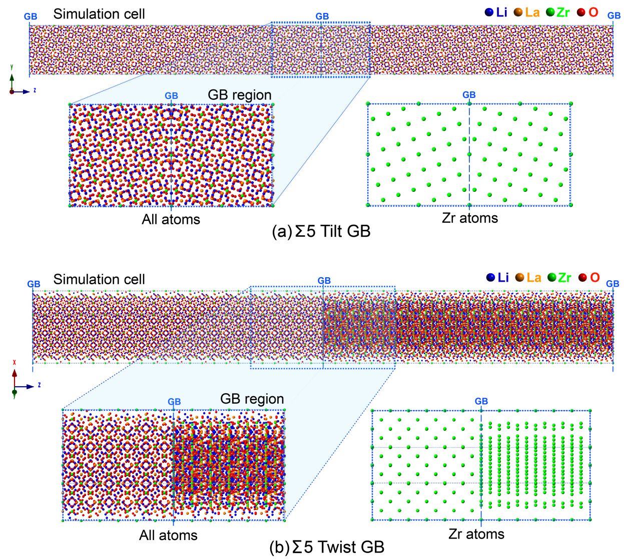

44

44

Validation of Interatomic Potential

The interatomic potential of Jalem gives reasonably good agreement with experimental and DFT-calculated elastic properties

Table 1. Calculated elastic constants, C_{ij}, and moduli (GPa) for cubic LLZO as a function of dopant and calculation method. The percent difference between DFT- and MD-predicted values for pure LLZO are given in parentheses.

System	Method	C_{11}	C_{12}	C_{44}	B	G	E
Al-doped LLZO	DFT (0 K)[a]	187	75	71	112	65	163
Al-doped LLZO	DFT (298 K)[a]					61	155
Al-doped LLZO	Experiment (298K)[a,b]				100.2, 102.8	58.1, 59.8, 59.6	146.1, 150.3, 149.8
Ta-doped LLZO	DFT (0 K)[a]	170	64	70	99	63	155
Ta-doped LLZO	DFT (298 K)[a]					59	147
Ta-doped LLZO	Experiment (298K)[a]				96.0	55.7, 61.2	139.9, 153.8
Pure LLZO	DFT (0 K)[c]	186	78	73	114	65	163
Pure LLZO	MD (0 K)[c], Adams[d]	190 (2 %)	115 (47 %)	29 (-60 %)	140 (23 %)	32 (-51 %)	90 (-45 %)
Pure LLZO	MD (0 K)[c], Klenk[e]	211 (13 %)	95 (22 %)	76 (4 %)	134 (18 %)	68 (5 %)	175 (7 %)
Pure LLZO	MD (0 K)[c], Jalem[f]	184 (-1 %)	79 (1 %)	60 (-18 %)	114 (0 %)	57 (-12 %)	146 (-10 %)

a: ref [9], b: ref[31], c: present study, d: ref [28], e: ref [29], f: ref [30]

45

45

Local Elastic Properties

GB elastic constants are up to ~50% smaller than bulk values

$\varepsilon_{33} = (L_z - L_{z,0})/L_{z,0}$

$C_{33} = \sigma_{33}/\varepsilon_{33}$

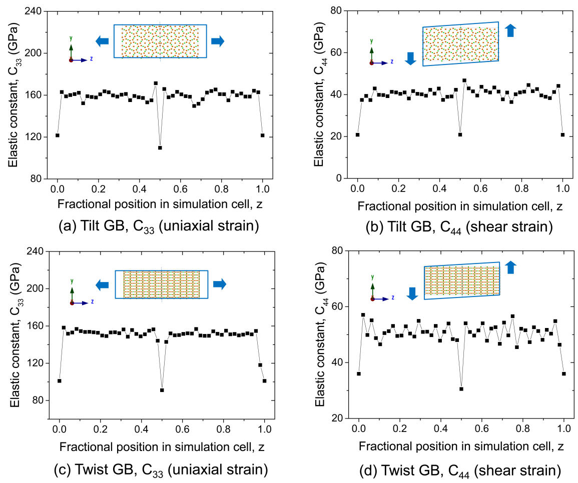

$\varepsilon_{44} = \Delta L_y/L_{z,0}$

$C_{44} = \sigma_{44}/\varepsilon_{44}$

Calculated elastic constants as a function of fractional position, z, at 300 K. (a, b) C_{33} and C_{44} for tilt GB, and (c, d) C_{33} and C_{44} for twist GB.

46

46

GBs in LLZO are Softer than the Bulk

GB elastic constants are up to ~50% smaller than bulk values

Elastic constant	Σ5 Tilt GB			Σ5 Twist GB		
	Bulk	**GB**	**Δ (%)**	**Bulk**	**GB**	**Δ (%)**
C_{33}, uniaxial	157	115	-27	150	95	-36
C_{44}, shear	39	21	-46	50	34	-32

- Accounting for the anisotropy of Li metal, G_{Li}[100] is nearly large enough to violate the Monroe/Newman criterion at GBs:
  - $G_{Li\text{-}bulk}$[100] = 10 Gpa (stiffest direction)
  - G_{LLZO}(GB) = 21 Gpa (softest GB)
- **Note:** interfacial porosity (G ~ 0 GPa) or microcracks could also serve as sites for dendrite initiation
- **Next steps**: quantify the effects of dopants and 2nd phases (Li_2CO_3) at GBs

Yu and Siegel, *Grain Boundary Softening: A Potential Mechanism for Lithium Metal Penetration Through Stiff Solid Electrolytes*
ACS Applied Materials & Interfaces, **10**, 38151–38158 (2018)
DOI: 10.1021/acsami.8b17223

47

47

Mechanisms of Inhomogeneous Plating

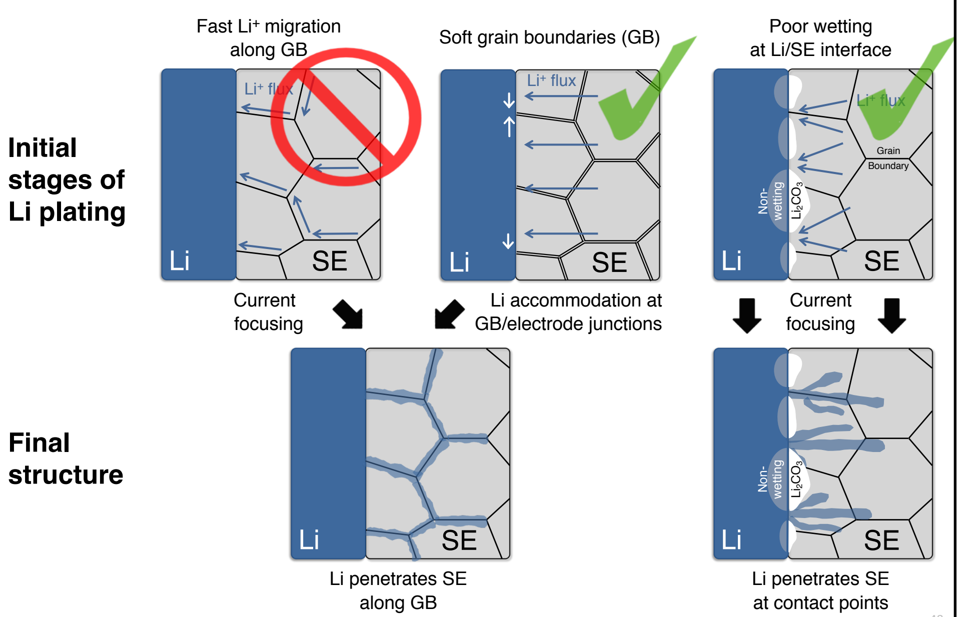

48

48

Acknowledgements

arpa·e

Financial support provided by the U.S. Department of Energy's Advanced Battery Material Research (BMR) program, grant DE-EE-00006821, and ARPA-e grant DE-AR0000653

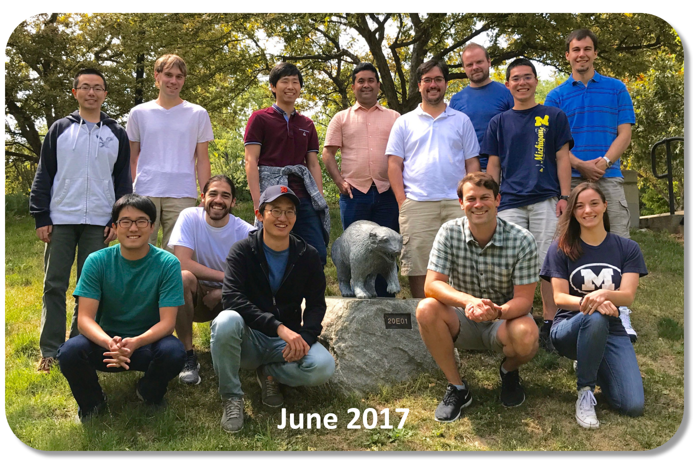

umich.edu/~djsiege
djsiege@umich.edu

49

49